12
Diffuse X-Ray Scattering at Low-Dimensional Structures in the System SiGe/Si

Michael Hanke

12.1
Introduction

In this chapter, we demonstrate the great potential of diffuse X-ray scattering to characterize low-dimensional structures. The related mesoscopic length scale is of high importance for semiconductors, since structures with nanometer extensions may exhibit quantum confinement. On the other hand, the driving forces of growth during epitaxy are most relevant at the mesoscopic length scale. They may drive self-formation and self-organization in a sense that those structures spontaneously form and assemble during growth. Certainly one of the most interesting and relevant objects are quantum dots (QDs) with zero-dimensional electronic properties and the resulting potential for optoelectronic devices.

Diffuse X-ray scattering is a well-established tool to probe morphology, for example, shape and size, as well as elastic strain, its relaxation, and positional correlation in vertical and lateral directions. Applying an integrating broad X-ray spot, this method provides in a nondestructive way structural information of an entire ensemble. In that X-ray scattering may serve in a complementary way to direct imaging techniques like transmission electron microscopy.

12.2
Self-Organized Growth of Mesoscopic Structures

Here, the term *mesoscopic* is used to characterize the length scale between the true *microscopic* regime (atomistic or subatomistic length scale) and larger *macroscopic* features. Usually it is applied to structures with dimensions from a few nanometers to about a couple of micrometers. This regime plays an outstanding role for semiconductors layers since typical exciton Bohr radii (and hence the necessary confinement) of semiconductors are in the range of a few tens of nanometers.

Mechanical Stress on the Nanoscale: Simulation, Material Systems and Characterization Techniques, First Edition.
Edited by Margrit Hanbücken, Pierre Müller, and Ralf B. Wehrspohn.
© 2011 Wiley-VCH Verlag GmbH & Co. KGaA. Published 2011 by Wiley-VCH Verlag GmbH & Co. KGaA.

Another important aspect is the fabrication of mesoscopic structures. In the past years, huge progress has been made in electron/ion beam and optical lithography. The fabrication of quantum wires or quantum dots is, however, still difficult since device applications have to fulfill several requirements. They have to be coherently grown on a substrate; that is, they must not contain any structural defects, such as misfit or threading dislocations. Also, high uniformity in size and shape has to be achieved. Moreover, a dense array of islands is needed. Lithographical techniques fulfill these requirements; however, the spatial resolution is still not sufficient to fabricate structures in the 20 nm regime.

12.2.1
The Stranski–Krastanow Process

At present, the most popular and promising approach is to make use of so-called self-organizing processes during growth; structures such as quantum dots and quantum wires spontaneously form during the epitaxial growth [1, 2]. Even in case of planar (layer by layer) epitaxy, growth proceeds by means of propagation of atomic steps. The typical terrace widths are in the mesoscopic range and, consequently, also the lateral correlation lengths of roughness [3]. Therefore, roughness is already a phenomenon of self-organization as it is strongly influenced by step–step interaction. For strained layers, the evolution of steps is mostly driven by strain relaxation that may lead to a step bunching (Asaro–Tiller–Grinfeld (ATG)) instability. Under certain growth conditions and sufficiently large surface miscut, these step bunches are quite narrow and regular. These systems may then serve as quantum wires.

Rather similar to strain induced step bunching is the so-called Stranski–Krastanow growth mode [4]. Under these growth conditions, first a couple of monolayers (wetting layer) grow layer by layer. This is followed by three-dimensional (3D) growth of coherent, defect-free islands. It is generally accepted that the equilibrium shape of such self-organized islands (often referred to as self-assembled islands) is determined by the balance of surface free energy and elastic strain energy [5]. Since real semiconductor surfaces are strongly anisotropic, the surface of the islands is often faceted, resulting in a complicated shape. Consequently, a large variety of shapes have been experimentally and theoretically reported [6–8]. Depending on the growth conditions, there can be, however, a remarkable influence of growth kinetics, for example, by limited surface diffusion lengths. Also, other factors, such as surface orientation, magnitude, and sign of strain, contribute to the complexity of growth. These complications of growth are the main reasons why self-organized growth is still not completely understood.

The above examples show that self-organization processes are most important at the mesoscopic length scale. This chapter focuses on arrays of self-organized nanoscale islands. Some of the structures reported here are still too large to show quantum size effects. However, the principles of self-organized growth remain the same as for quantum dot structures. These growth principles are present in

the entire mesoscopic range, that is, for structure extensions from a few nanometers to about 1 μm.

12.2.2
LPE-Grown $Si_{1-x}Ge_x$/Si(001) Islands

For a monodisperse island distribution, it can be shown that the X-ray scattering signal originating from the ensemble decouples in reciprocal space into a simple product (scattering by a single island times a correlation function) [9]. In that context, freestanding $Si_{1-x}Ge_x$ islands grown by liquid-phase epitaxy (LPE) [10] on Si(001) substrates may serve as an ideal model system. These samples consist of coherent, highly monodisperse islands with uniform shape and composition. As depicted in Figure 12.1, the islands are shaped like truncated pyramids with $\{111\}$ side facets and a (001) top facet. Another advantage is the ability to tune the island size w: as outlined in Ref. [11], the island base width w is closely related to the lattice mismatch f between $Si_{1-x}Ge_x$ and Si (and consequently—via Vegard's law—to the germanium content x) according to $w \propto f^{-2}$.

All these properties of LPE-grown SiGe islands make them suitable as a model system that allows demonstrating the excellent potential of X-ray diffuse scattering for structural characterization. On the other hand, LPE-grown $Si_{1-x}Ge_x$ islands are interesting with respect to a detailed understanding of self-organized growth. They are especially perfect in above sense when the growth conditions are chosen comparatively close to thermodynamic equilibrium. This sheds some light on the frequently discussed question of to what extent the Stranski–Krastanow growth mode can be discussed in terms of total energy minimization [5] and whether kinetic processes may play a crucial role.

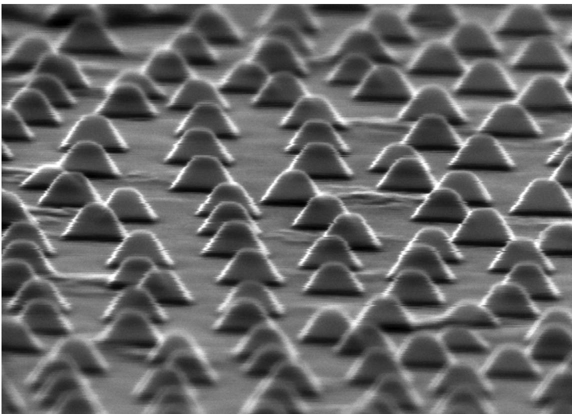

Figure 12.1 Scanning electron micrograph of $Si_{0.70}Ge_{0.30}$ nanoscale islands grown on (001) Si by LPE. The islands have the shape of truncated pyramids with $\{111\}$ side facets and a (001) top facet. The island base width is about 130 nm.

12.3
X-Ray Scattering Techniques

The essential part of the diffuse scattering of mesoscopic structures is found close to reciprocal lattice points. This requires high angular resolution and a monochromatic beam. These techniques are, therefore, referred to as high-resolution X-ray methods. On the other hand, since the penetration depth of X-rays in semiconductor material is of the order of several tens of micrometers, the diffusely scattered signal from mesoscopic structures is usually rather weak. For that reason, a very intense X-ray source is necessary. Both high intensity and high resolution are achieved through the use of brilliant synchrotron radiation. A crystal monochromator selects a rather narrow wavelength band $\Delta\lambda/\lambda$ of typically 10^{-4}, whereby the angular divergence of the beam is of the same order (in radians). The direction of the diffracted beam can be analyzed in different ways:

1) Single channel detector combined with a collimating slit system
2) Linear position-sensitive detector (PSD)
3) Two dimensionally resolving, position-sensitive CCD detectors
4) Crystal analyzer

The actual choice depends on the scattering geometry and, thereby, on the required resolution, the dynamical range, and the area of interest in reciprocal space. For example, a crystal analyzer gives the best resolution, but a high-resolution mapping in reciprocal space is also very time-consuming. For sufficiently small spot sizes at the sample, the use of position-sensitive detectors (PSD or CCD) could be rather advantageous [12]. In this case, different channels of the PSD correspond to different angles of the scattered beam. The angular distribution of scattered wave vectors can therefore be simultaneously recorded. This multidetection technique substantially reduces the data acquisition time. At spot sizes in the range of 200 μm and a distance between sample and detector of about 1000 mm, the angular resolution of the diffracted beam is of order $\Delta\Theta = 2 \times 10^{-4}$ rad. This intermediate resolution—though definitely worse than the high resolution provided by a crystal analyzer—often turns out to be sufficiently good for the analysis of diffuse scattering.

12.3.1
High-Resolution X-Ray Diffraction

We use the term HRXRD (high-resolution X-ray diffraction) for all diffraction geometries where

1) the reciprocal lattice vector fulfills the condition $\mathbf{q} \neq 0$ and
2) the incident and exit angles with respect to the sample surface are large compared to the critical angle of total external reflection.

Since the scattered intensity depends on the scattering vector $\mathbf{q}$, the reciprocal space can be probed by setting appropriate directions of the incident and scattered beams (Figure 12.2). This geometry is referred to as "extended Ewald sphere

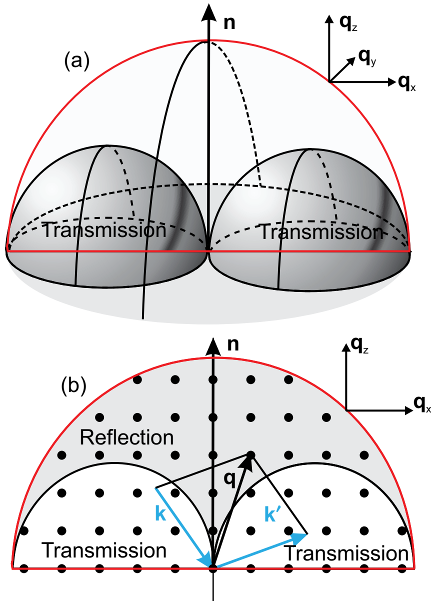

Figure 12.2 Scheme of reciprocal space. (a) Represents the half-sphere in reciprocal space accessible through a fixed wavelength λ. (b) Gives a 2D cut containing the surface normal **n**. The reciprocal lattice points are marked by black dots. The radius of the large sphere is $r = 2k = 4\pi/\lambda$. The cut is chosen to contain the wave vectors **k** and **k**′ of the incident and scattered waves, respectively. This 2D cut is thus identical with the scattering plane. In addition, the sample normal vector **n** lies in the scattering plane (coplanar scattering). The white areas are accessible only in transmission geometry, for example, by a vector **k**′ pointing into the crystal. By systematically varying the directions of **k** and **k**′, the scattering vector **q** maps out different areas in reciprocal space.

construction." In Figure 12.2b, a two-dimensional cut through reciprocal space is shown. The usage of a PSD in this plane will correspond to a "scan" in reciprocal space along a line. A two-dimensional detector corresponds to multitude of scans in an analogous curved plane. To map the reciprocal space in three dimensions (3D), a combination of above components is often used. Since the mesoscopic structures under consideration are located close to the sample surface, reflection geometry ("Bragg case") is the best choice. This corresponds in Figure 12.2 to the white area inside the half-sphere with radius $r = 2k = 4\pi/\lambda$.

12.3.2 Grazing Incidence Diffraction

This is similar to HRXRD, that is, $\mathbf{q} \neq 0$; however, the incoming X-rays hit the surface under a very small angle of incidence, typically a few tens of a degree. Thus, the scattering plane is not necessarily perpendicular to the sample surface. A special case of grazing incidence diffraction (GID) refers to the fact that both incident and

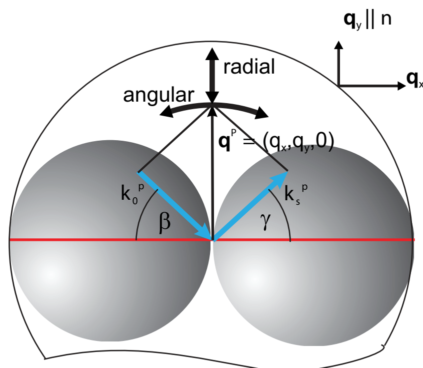

Figure 12.3 In-plane GID geometry. Both smaller half-spheres indicate the Laue case. The incoming X-rays hit the surface under a very small angle of incidence and are diffracted at vertically aligned diffraction planes in the crystal. By changing the angles β and γ, one may move the target point of the diffraction vector along **q**, which is the *radial* direction, while an *angular* scan probes intensity in a perpendicular direction.

exit X-ray beams hit the surface under very grazing angles. A typical setup is shown in Figure 12.3. In this geometry, refraction effects are important. Since the refraction index of X-rays is slightly below 1, total external reflection occurs below a critical glancing angle, α_c, and the X-ray penetration depth shrinks to a few nanometers. Slightly above the critical angle, the penetration depth is about a factor of 100 larger. Therefore, GID enables to tune the information depth from a few nanometers up to a few hundreds of nanometers. Since mesoscopic structures are often buried at comparative depths, the use of GID leads to an enhanced sensitivity compared to HRXRD. However, the information on lattice strains accessible via GID is restricted to the horizontal strain tensor components.

Similar to HRXRD, different ways of analyzing the diffracted beam are possible. Often, a position-sensitive detector oriented perpendicular to the surface is used to record different values of exit angles with respect to the surface (see Figure 12.3). The in-plane component of the diffracted beam is measured by using an analyzer crystal between sample and PSD. With that geometry, a 3D mapping of reciprocal space is possible. A comprehensive introduction to GID is given in Ref. [13].

12.3.3 Grazing Incidence Small-Angle X-Ray Scattering

HRXRD and GID record the diffuse intensity in the vicinity of an arbitrary reciprocal lattice point with $\mathbf{q} \neq 0$. This leads to large scattering angles. By contrast, the corresponding scattering angles in the proximity of $\mathbf{q} = 0$ are rather small. This case is, thus, referred to as small-angle X-ray scattering (SAXS). There is no influence of strain and thus only electron density fluctuations are probed. Since the mesoscopic structures are usually deposited onto a thick substrate, the usual SAXS transmission geometry is not suitable here and a reflection geometry is chosen. To accumulate

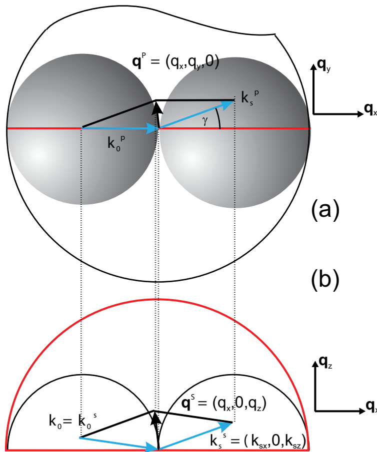

Figure 12.4 GISAXS geometry (a) projected on the q_x–q_y plane and (b) a cut of the q_x–q_z plane. Although the lateral component of **q** is restricted by the Laue spheres for small incidence and exit angles (b), this limitation is not present in-plane (a).

sufficient signal, the corresponding angles of incidence and exit are chosen rather small. Figure 12.4 shows a schematic view of the scattering geometry. Here, the diffuse intensity may be recorded by a CCD detector or, alternatively, by a combination of a crystal analyzer and a PSD. By azimuthally rotating the sample, the entire three-dimensional intensity distribution of diffuse scattering in the vicinity of $\mathbf{q} = 0$ can be recorded. Nearly the same setup is used for X-ray reflectometry. However, in case of reflectometry, only the intensity of the specularly reflected beam is measured.

12.4 Data Evaluation

In case of an (at least) partly incoherent diffraction, it is impossible to directly retrieve the required information from X-ray diffuse scattering. Some of them are the loss of phase information by intensity measurement, the tensor character of strain, and the superimposition of effects of strain, shape, and positional correlation. Therefore, for reasons of simplicity, analytical expressions are frequently used to approximate the strain field. Owing to the complicated strain tensor field $\varepsilon_{ij}(x, y, z)$ of a three-dimensional island, this approach is not justified anymore. In the last years, the finite element method (FEM) has been successfully established to solve the problem. FEM is based on linear continuum elasticity theory and has proven to be applicable down to structure sizes of a few tens of nanometers. At object sizes below about 20 nm and at very high lattice mismatch (e.g., 7% for InAs QDs on GaAs), there are distinct deviations from elasticity theory and the atomic structure of the QDs has to be considered. For the systems discussed here, elasticity theory is valid and the following iterative approach [14] for data evaluation of nanoscale islands can be applied:

1) Creation of specific structure model in real space that includes island size, shape, and chemical composition.
2) FEM calculation of the entire three-dimensional strain field inside the island and surrounding the substrate and wetting layer.
3) Numerical simulation of diffuse scattering.
4) Comparison with experimental data.
5) Further improvement of the model created in the first step and respective calculation of diffuse intensities until satisfying agreement is achieved.

In general, this approach cannot be used as a fitting procedure since there are too many free parameters in the model (shape, size, composition, spatial correlation). Therefore, it is necessary to include knowledge obtained by other methods, for example, information on shape and size by AFM, scanning electron microscopy (SEM), and TEM. First, the calculation is done for a single island and its environment. The subsequent simulation of diffuse intensity is performed numerically, that is, on a regular grid consisting of *super cells*. If it is necessary, the dimension of base cells can be chosen as small as that of crystal unit cells; however, they can be also chosen larger. The numerical procedure has to be done for some 10^6–10^7 base cells and more than 10^4 values of $\mathbf{q}$ and is therefore rather time-consuming.

In the following section, at selected examples it will be demonstrated how structural properties such as strain, shape, size, and positional correlation of the mesoscopic structures can be evaluated from diffuse scattering.

12.5 Results

The X-ray diffuse scattering that one is interested in is expected to show a rather low signal. Therefore, conventional X-ray sources are not suitable for that task. For that reason, measurements were performed using intense synchrotron radiation at HASYLAB (Hamburg, Germany) and ESRF (Grenoble, France). Typical X-ray wavelengths of $\lambda = 1.5$ Å have been chosen.

First, it will be demonstrate how shape and size of nanoscale islands can be extracted from GISAXS data and how these compare to respective AFM measurements. Then, we will demonstrate how strain and composition changes can be extracted from HRXRD. In the data evaluation, respective information about shape and lateral correlation as evaluated before has to be used. Later, the interplay between the island shape and the strain inside the island will be highlighted.

12.5.1 The Influence of Shape and Size on the GISAXS Signal

As explained before, the present way of strain evaluation presumes prior knowledge regarding island shape. In case of freestanding islands, the shape can be evaluated by using AFM or SEM and by GISAXS as well. Thus, freestanding islands are well suited

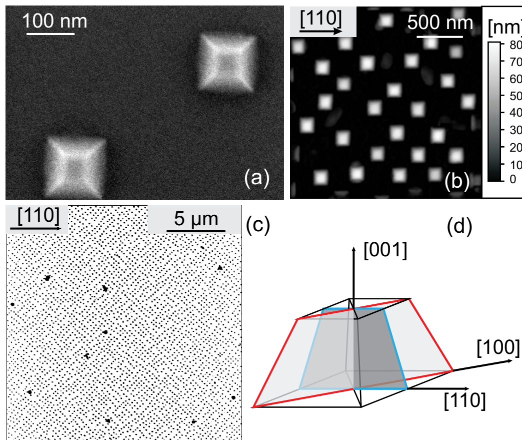

Figure 12.5 Atomic force (b, c) and scanning electron (a) micrographs of $Si_{0.70}Ge_{0.30}$ nanoscale islands grown on (001) Si by LPE. (d) The orientation of two particular scattering planes containing the [110] or the [100] direction.

to compare results achieved by direct imaging (AFM, SEM) and X-ray diffuse scattering.

In Figure 12.5b and c, AFM micrographs of an ensemble of $Si_{0.7}Ge_{0.3}$/Si(001) islands are compared with a respective scanning electron micrograph (Figure 12.5a) recorded at a different position of the same sample. AFM provides information on island shapes and positional correlation. However, the exact island shape information is blurred due to tip convolution. SEM reveals more detailed information on the island shape due to the small beam size of the scanning electron beam. However, complete shape information is accessible only in plane view (Figure 12.5b) and side view (e.g., Figure 12.1) of the sample. The plane view shown here provides additional information on positional correlation.

The 3D shape of a single island leads to a respective 3D intensity distribution in reciprocal space. However, in view of the known symmetry of the island, two different 2D cuts within two nonequivalent mirror planes of the island are sufficient in our case. 2D means that the scattering vector **q** maps out a plane in reciprocal space. This is schematically illustrated in Figure 12.5d. Both scattering planes (shaded) are oriented perpendicular to the sample surface and contain [110] or [100] vector, respectively.

The GISAXS signal consists of two main components: the first factor $|\Omega^{FT}(\vec{q})|^2$ arises from the shape function $\Omega(\vec{r})$ of a single island, whereas the second one describes positional correlation between different islands. Calculations of $|\Omega^{FT}(\vec{q})|^2$ for a truncated pyramid displayed in Figure 12.5d are shown in Figure 12.6c and d. Two remarkable features are discussed here:

1) There are extended streaks (marked F) that are collinear with the surface normal of the $\{111\}$ side facets (indicated by dashed lines) and with the (001) top facet. In the literature, these streaks are often referred to as crystal truncation rods (CTR) since they appear due to the truncation of a three-dimensional object by a flat surface. The existence of CTRs is quite useful to identify faceting of mesoscopic structures.

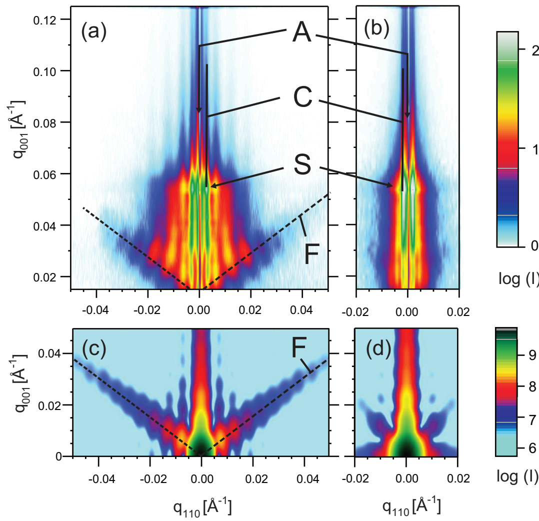

Figure 12.6 Measured GISAXS patterns at SiGe/Si(001) islands within different crystallographic zones containing the [110] direction (a) or the [100] direction (b) in comparison to kinematic scattering simulations (c, d). "F" indicates the inclination of the facet rods, "S" the position for the specularly reflected beam, "C" the presence of correlation peaks, and "A" an absorber artifact.

Their widths inversely scale with the corresponding extension of the facets in real space and thus contain valuable information about structure dimensions.

2) In Figure 12.6c, the intensity distribution is horizontally modulated. These fringes are caused by the finite size of the island. Their mutual spacing in reciprocal space inversely scales with the island size.

The intensity distribution in Figure 12.6c and d can be compared with experimental GISAXS measurements as shown Figure 12.6a and b. In the experimental data, streaks along the {111} directions appear, and their intensity modulations correspond to that in the simulation. The agreement between experiment and simulation is best for a truncated pyramid with $w = 130$ nm and $h = 78$ nm. However, significant differences are present:

1) The experimental streaks merge at about $q_z = q_{001} = 0.027\,\text{Å}^{-1}$, whereas the kinematically simulated streaks merge at $q_x = q_{001} = q_{110} = 0$. Moreover, the {111} streaks are bowed.
2) In the kinematic simulations, the specularly reflected beam is missing.
3) Close to the specular beam, strong correlation satellites appear that show a rodlike intensity distribution.

Positional correlation is not a serious problem. In most cases—when the mean distance of mesoscopic structures is much larger than their lateral size—the satellite peaks (rods) can be well distinguished from shape-induced diffuse scattering. Positional correlation can be then described by a correlation function. Refraction

effects are implemented in the theoretical descriptions by using distorted wave Born approximation (DWBA). As noticed before, the most serious problem is the theoretical treatment of the specular beam, which is missing in kinematic theory. This beam can also undergo small-angle scattering, leading to enhanced intensity in its close vicinity, as visible in Figure 12.6a and b at about $q_{001} = 0.06\,\text{Å}^{-1}$.

12.5.2
HRXRD Measurement of Strain and Composition

So far we have concentrated on the diffuse scattering around the origin of reciprocal space, that is, $\mathbf{q} = 0$ (GISAXS), which is insensitive to strain and essentially probes electron density fluctuations. In the case of HRXRD ($\mathbf{q} \neq 0$), the diffuse scattering contains additional information on strain, while the information on shape and positional correlation is retained. Without any strain, the diffuse scattering close to a reciprocal lattice point should be similar to that shown in Figure 12.6. Actually, the diffuse scattering looks quite different and is dominated by strain effects. This is demonstrated in Figure 12.7, where the diffuse intensity in the vicinity of the 004 reciprocal lattice point is displayed for SiGe islands on Si as given in Figure 12.5.

To understand the general features of strain-induced diffuse scattering, some prior considerations regarding strain in such islands have to be made. In the framework of linear elasticity theory, the strain distribution explicitly depends on the lattice mismatch; that is, any change in the Ge content causes a respective linear change of strain, as given by Vegard's law. With any change of size, the strain distribution is simply rescaled. In other words, the island size does not influence the "symmetry" of the strain distribution, which instead depends on the symmetry of the island shape. The island size, on the other hand, has no impact on the qualitative behavior of the strain field and hence the diffuse scattering. Thus, the qualitative features shown in Figure 12.7 are characteristic of a truncated pyramid of any size. This useful scaling behavior of linear elasticity theory can be used to distinguish between strain, shape, and size related diffuse scattering.

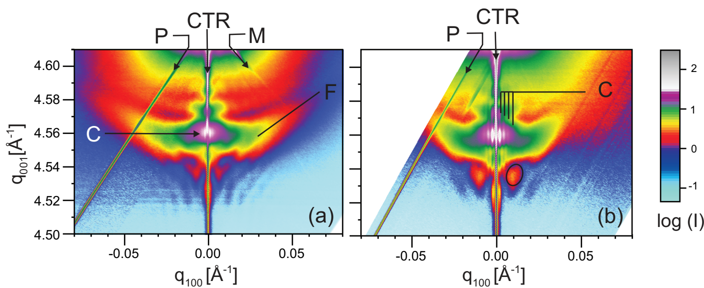

Figure 12.7 Diffusely scattered intensity by a SiGe/Si island ensemble near the 004 reflection. Both distributions differ by the respective scattering plane, which contains the [110] or the [100] direction. CTR denotes the crystal truncation rod, which is accompanied by correlation peaks (C); P and M denote a detector artifact and the monochromator streak, respectively.

On the basis of the FEM calculations, one can roughly divide the island into two parts: a strongly strained base and a nearly completely relaxed top part. These two components can be also observed in the diffuse scattering. Since the top part is practically totally relaxed, the respective diffuse scattering is given by a rather sharp central peak at around $q_{001} = 4.56\,\text{Å}^{-1}$. The complex interplay between several strain tensor components toward the island edges is responsible for the butterfly-shaped feature of the diffuse intensity in Figure 12.7. Here, both the diagonal and nondiagonal components of the strain tensor and local tilts of atomic planes are playing a crucial role. Since the wings of the butterfly are present in both (a) and (b), it is evident that they are not caused by the island shape function as shown in Figure 12.6. There are indications of the influence of the island shape manifested in a rich variety of "thickness fringes." The clear discrepancy between Figures 12.6 and 12.7 proves, however, that the diffuse intensity measured by HRXRD is dominated by strain effects.

Applying the kinematic approach, the diffuse scattering can be calculated by adding up the scattering of all illuminated scatterers. This approach is based on the strain field derived from FEM calculations of a single island. Since the shape and size of island are known, the only remaining free parameter is the Ge concentration profile $c(r)$ inside the island. There is no satisfying agreement between the experimental data (Figure 12.7) and the simulation for a homogeneous island, that is, $c(r) = c = \text{const}$, as can be seen in Figure 12.8a. Different profiles for $c(r)$ have been tested [15]. Surprisingly, an abrupt vertical change at about one-third of the island height (Figure 12.8b) yields better results than smooth vertical gradients (not shown here). By systematically varying the vertical position of the interface and the concentration (also not shown), one can estimate the accuracy to about 5 nm, whereas the uncertainty in the concentration amounts to about $\pm 2\%$ Ge. A more complicated three-dimensional composition gradient as shown in Figure 12.8c does not further improve the agreement to experiment.

The simulations shown above prove the high sensitivity of diffuse scattering on very small composition changes. The relative change in electron density—and thus in the structure amplitude—induced by this abrupt composition change is only 2.5%. The diffuse scattering is not sensitive to such small changes in the structure factor, and, consequently, they cannot be detected by GISAXS. However, they can be probed by HRXRD since the influence of the abrupt Ge composition change on the strain distribution is large enough to induce characteristic features in the diffuse scattering as can be seen when comparing Figure 12.8a and b. The accuracy of the position of the abrupt change is approximately $z/h = 5\%$ of the island height.

12.5.3
Positional Correlation Effects in HRXRD

Figure 12.8a–c display simulated diffuse scattering maps of single islands; that is, positional correlation is not included in these calculations. It is, however, known from the GISAXS and AFM measurements (Figure 12.6) that there are strong correlation effects and, indeed, they are also visible in Figure 12.7 as strong vertical satellite rods

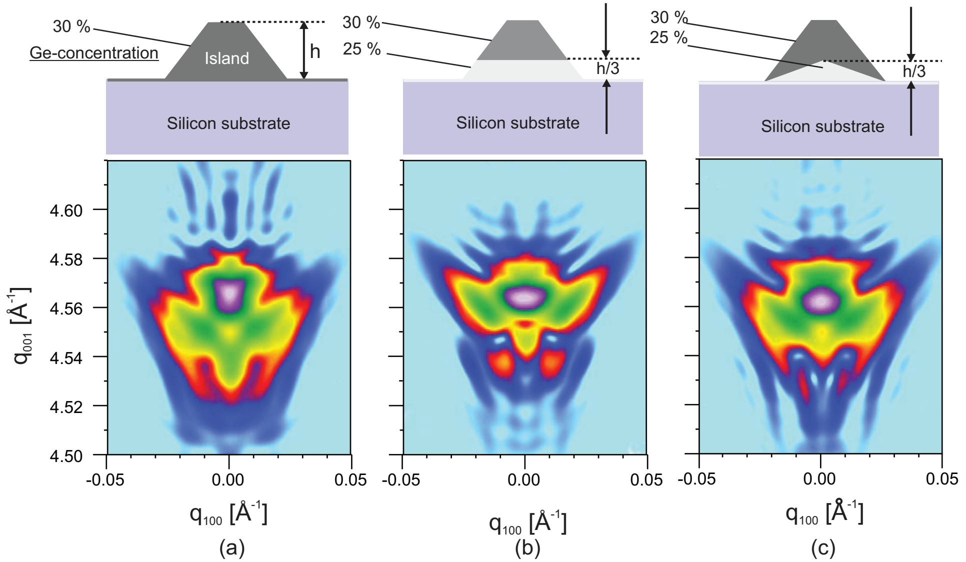

Figure 12.8 2D HRXRD simulations of the diffuse scattering from a single SiGe island close to the 004 reciprocal lattice point of the Si substrate. The horizontal scattering vector is parallel to [100]. (a) Homogeneous Ge composition, $c = 30\%$. (b) Abrupt vertical change in Ge composition at one-third of the island height with $c_1 = 25\%$ in the lower part and $c_2 = 30\%$ in the upper part. (c) Respective abrupt change in Ge composition with a flat pyramidal interface.

(marked C) parallel to the main rod at $q_x = 0$. They are especially intense in the vicinity of the central peak. In agreement to GISAXS, the correlation peaks are remarkably pronounced in $\langle 100 \rangle$ direction. The positional correlation can be easily implemented into the theoretical simulations for diffuse scattering [9]. According to the finite coherence length of the applied X-ray radiation, a numerical, partly coherent and incoherent correlation function G has been used, whereby an excellent agreement between simulation (Figure 12.9b) and experiment (Figure 12.9a) can be achieved. The good correspondence can be also checked for a horizontal cut through simulation and experiment as shown in Figure 12.9c.

12.5.4 Iso-Strain Scattering

Grazing incidence diffraction is sensitive to the horizontal strain tensor components (i.e., ε_{xx}, ε_{xy}, and ε_{yy}) if both incidence and exit angles are small. Therefore, this scattering geometry seems to be not suitable to probe vertical composition changes as could be detected by HRXRD. Nevertheless, since the horizontal strain tensor component $\varepsilon_{xx}(\vec{r})$ monotonically increases with the vertical position inside the island [14], it is possible to monitor the horizontal strain as a function of the vertical position inside the island. Therefore, the island profile has to be known.

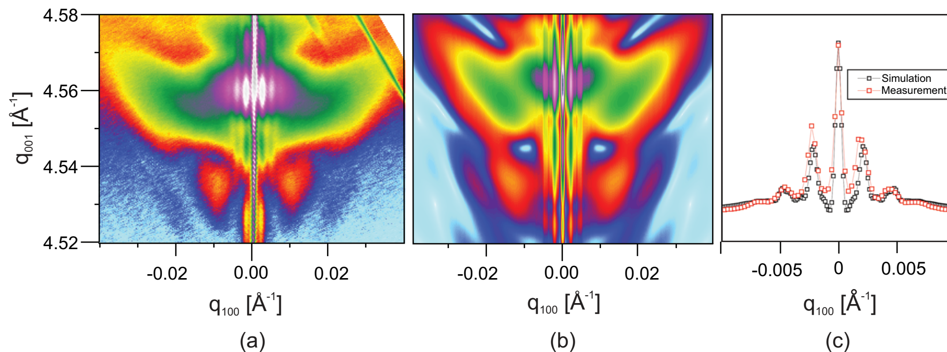

Figure 12.9 2D HRXRD measurement (a) and simulation (b) of diffuse scattering at an ensemble of SiGe islands close to the Si(004) reciprocal lattice point. The horizontal scattering vector is parallel to [100]. Positional correlation is included in the simulations by using a correlation function extracted from AFM. (c) A horizontal cut through simulation and experiment at $\mathbf{q}_{001} = 4.563\ \text{A}^{-1}$.

This technique has been referred to as "iso-strain scattering" and "X-ray tomography" and was first introduced by Kegel *et al.* [16]. It is not possible to go into detail with that procedure, but the basic idea behind this approach will be briefly discussed in the following. First, consider the two different scan directions q_{radial} and q_{angular} (as defined in Figure 12.3):

1) The diffuse intensity along radial scattering vector q_{radial} is mostly sensitive on the horizontal strain tensor component along this direction, for example, ε_{xx}. Increased values of ε_{xx} then show up in diffuse intensity at decreased values of q_{radial} and vice versa. The diffuse intensity extended along the direction of q_{radial} can, thus, be assigned to different values of ε_{xx}.
2) The dependence of diffuse intensity on q_{angular} is mainly determined by the horizontal island shape and size, and it is practically insensitive to ε_{xx} ($= \varepsilon_{yy}$). Therefore, distinct "thickness fringes" (marked as d in Figure 12.10) should be observed in the direction of q_{angular}.

As already stated, the lateral strain component ε_{xx} is a monotonic function of the vertical position z inside the island. Therefore, the values of q_{radial} can be assigned to respective vertical positions z inside the island. On the other hand, increasing vertical positions inside the island leads to decreasing horizontal island width and, thus, to increased distances between the fringes (d). This is exactly what is observed experimentally in Figure 12.10a: with decreasing values of q_{radial}, we probe higher parts of the island. These higher parts exhibit a smaller horizontal width, leading to thickness fringes with larger period.

We have to note, however, that a quantitative evaluation is difficult, since the horizontal strain at a certain vertical position z is not constant but depends on x and y. The areas of constant horizontal strain ("iso-strain areas") inside the island are bowed. It has been shown [16] that the iso-strain areas can be determined experimentally and can be used to determine a composition gradient in nanoscale islands.

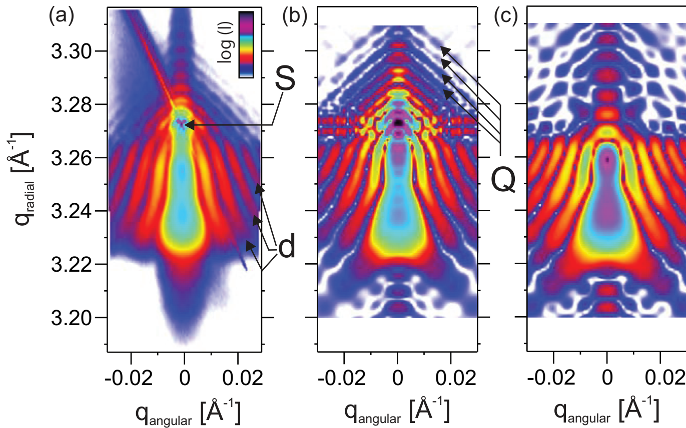

Figure 12.10 In-plane GID intensity near the Si(220) reflection (S) as measured (a) and simulated including scattering from island and substrate (b) and pure island scattering (c). Thereby, different contributions by the island (d) and the strained substrate (Q) become pronounced.

However, this procedure works only for rotationally symmetric objects and cannot be applied to truncated pyramids as discussed here.

Figure 12.10b and c represent two kinematic simulations with the same parameters as used in Figure 12.8b and a good agreement with experiment is achieved. While simulation (b) shows scattering contributions by the island and the substrate (which is in particular visible by the reproduced fringes *Q*), simulation (c) just gives the scattering by the island itself. Surprisingly, the simulations are not as sensitive to vertical composition changes as with HRXRD. There are some distinct differences of the experimental and theoretical intensity distributions in radial direction that can probably be explained by multiple scattering processes. To reproduce all details in the experimental map, a more sophisticated theoretical approach including the DWBA has to be developed.

12.6 Summary

The mesoscopic length scale plays an outstanding role in semiconductors. On the one hand, quantum size effects appear at structure dimensions of typically a few tens of nanometers. On the other hand, the driving forces during growth of these structures are most relevant at mesoscopic length scales and they may lead to self-organization processes in that structures can form spontaneously during epitaxial growth. Among these processes is the Stranski–Krastanow growth mode that leads to three-dimensional coherent island structures showing pronounced strain-induced positional correlation.

The great potential of X-ray diffuse scattering for the characterization of mesoscopic structures has been discussed. Owing to the high angular resolution of X-rays,

the entire mesoscopic length scale is accessible by X-ray scattering. Selected examples have demonstrated the capabilities of different scattering techniques. Among them are HRXRD, GID, and grazing incidence small-angle X-ray scattering (GISAXS). The latter is solely sensitive to electron density fluctuations. Among these are the island shape and positional correlation that can be distinguished in the diffuse intensity. HRXRD and GID are sensitive to these, but they are also sensitive to the three-dimensional strain field inside and in the vicinity of the islands. We have evaluated our data in the framework of kinematic theory and have also discussed the limits of that approach.

A data evaluation procedure that uses the FEM is briefly introduced. This allows evaluation of the complex strain field inside nanoscale islands. As an important result of that technique, we were able to detect an abrupt Ge composition change inside LPE-grown SiGe islands. Positional correlation can easily be included in the simulations by the use of the pair correlation function G.

References

1 Bimberg, D. (2008) *Semiconductor Nanostructures*, Springer.
2 Schmidt, O.G. (2007) *Lateral Alignment of Epitaxial Quantum Dots*, Springer.
3 Kondrashkina, E.A., Stepanov, S.A., Opitz, R., Schmidbauer, M., Köhler, R., Hey, R., Wassermeier, M., and Novikov, D.V. (1997) *Phys. Rev. B*, **56**, 10469.
4 Stranski, I.N. and Krastanow, L. (1937) Sitzungsberichte d. Akademie d. Wissenschaften in Wien, Abt. IIb, Band 146, 797.
5 Hanke, M., Schmidbauer, M., Syrowatka, F., Gerlitzke, A.K., and Boeck, T. (2004) *Appl. Phys. Lett.*, **84**, 5228.
6 Ballet, P., Smathers, J.B., Yang, H., Workman, C.L., and Salamo, G.J. (2000) *Appl. Phys. Lett.*, **77**, 3406.
7 Chaparro, S.A., Zhang, Y., and Drucker, J. (2000) *Appl. Phys. Lett.*, **77**, 3406.
8 Lorke, A., Luyken, R.J., Govorov, A.O., Kotthaus, J.P., Garcia, J.M., and Petroff, P.M. (2000) *Phys. Rev. Lett.*, **84**, 2223.
9 Hanke, M., Schmidbauer, M., and Köhler, R. (2004) *J. Appl. Phys.*, **96**, 1959.
10 Teubner, T. and Boeck, T. (2006) *J. Cryst. Growth*, **289**, 366.
11 Dorsch, W., Strunk, H.P., Wawra, H., Wagner, G., Groenen, J., and Carles, R. (1998) *Appl. Phys. Lett.*, **72**, 179.
12 Schmidbauer, M., Schäfer, P., Besedin, S., Grigoriev, D., Köhler, R., and Hanke, M. (2008) *J. Synchroton Rad.*, **15**, 549.
13 Pietsch, U., Holy, V., and Baumbach, T. (2004) *High-Resolution X-Ray Diffraction*, Springer, New York.
14 Hanke, M., Schmidbauer, M., Grigoriev, D., Raidt, H., Schäfer, P., Köhler, R., Gerlitzke, A.K., and Wawrak, H. (2004) *Phys. Rev. B*, **69**, 075317.
15 Hanke, M. and Boeck, T. (2006) *Physica E*, **32**, 69.
16 Kegel, I., Metzger, T.H., Peisl, J., Stangl, J., Bauer, G., Nordlund, K., Schoenfeld, W.V., and Petroff, P.M. (2001) *Phys. Rev. B*, **63**, 03531.